ADVANCED FUNCTIONAL MATERIALS
www.afm-journal.de

Metallic Sliding Ferroelectricity in Trilayer Penta-NiN_2

*Changsheng Hou, Yiheng Shen, and Qian Wang**

The experimental observation of metallic ferroelectricity has challenged the traditional understanding in recent years, as metallicity and ferroelectricity are historically considered mutually exclusive. This breakthrough has sparked significant interest in this field. However, the coexistence of metallicity and sliding ferroelectricity in 2D pentagonal materials has not been reported yet. Here, this is theoretically studied that the sliding ferroelectricity in metallic trilayer penta-NiN_2. By scanning the configuration space of stacking patterns, a pair of polarized configurations is identified with strong out-of-plane ferroelectric polarization of $\pm 5.39 \times 10^{-13}$ C m^{-1} and a low polarization switching barrier of 14.33 meV/atom together with a non-polarized configuration as the intermediate state for the ferroelectric transition. It is also found that there are substantial changes in the second harmonic generation of the stable configurations that would facilitate experimental observation. This work demonstrates the potential of pentagonal sheets as promising metallic sliding ferroelectrics, which would significantly expand the family of sliding ferroelectric materials.

1. Introduction

Atomic-thin 2D ferroelectric materials provide a unique platform for multifunctional miniaturized devices[1] due to the switchable polarization under an external electric field. However, most 2D materials with centrosymmetric nature in their monolayers do not exhibit ferroelectric properties. Thus, 2D intrinsic ferroelectrics are restricted to a few materials, such as $CuInP_2S_6$,[2] α-In_2Se_3,[3] SnTe,[4] and SnSe.[5] In order to overcome such limitations, sliding ferroelectricity was proposed in 2017,[6] which has significantly expanded the family of 2D ferroelectric materials, giving rise to a new research field known as slidetronics. Different from the mechanism of conventional ferroelectrics, which arises from the ion displacement via overcoming high energy barriers resulting from strong chemical bonds, sliding ferroelectricity involves surmounting only the weak van der Waals (vdW) forces between the layers,[7] leading to much lower switching barriers than conventional ferroelectrics, which is associated with their feasibility of room-temperature operation[8] and fatigue-free performance.[9] Such fascinating ferroelectricity has been observed in amphidynamic crystal,[10] bilayer and multilayer BN,[11] γ-InSe,[12] WTe_2,[13] MoS_2,[14] and $MoTe_2$,[15] etc. According to the generalized group theory for bilayer sliding ferroelectricity (BSF) theory proposed recently,[16] more sliding ferroelectric materials could be rationally designed for better performance.

Among the unique features of sliding ferroelectrics, the coexistence of ferroelectricity and metallicity observed in metallic bilayer and trilayer WTe_2[13] gives rise to metallic sliding ferroelectricity due to the lack of conducting channel in the out-of-plane direction with broken periodicity. Subsequent research uncovered unconventional superconductivity and nonlinear anomalous Hall effect in multilayer WTe_2,[17] adding to the practical significance of sliding ferroelectrics. Moreover, further study on the mechanisms of metallic sliding ferroelectricity in WTe_2 bilayer and multilayer was also carried out.[18] However, WTe_2 is the only experimentally synthesized system reported so far with metallic sliding ferroelectricity, and the rational design of sliding ferroelectric materials is still in its early stages.

Since the proposal of penta-graphene (PG) in 2015,[19] considerable efforts have been dedicated to the rational design and experimental synthesis of over 170 new 2D pentagonal materials.[20,21] The unique geometry of such pentagonal materials allows for the emergence of spontaneous polarization and intrinsic ferroelectricity as reported in some 2D materials composed entirely of pentagonal motifs.[22–24] Furthermore, an in-plane sliding ferroelectricity was recently identified in the penta-$PdSe_2$/penta-$PtSe_2$ vdW heterostructure,[25] which could be experimentally prepared via symmetry-driven epitaxy.[26] These research advances raise the following question: is it possible to design metallic sliding ferroelectricity using the multilayers of readily synthesized pentagonal materials? In this work, motivated by the synthesis of penta-NiN_2, a pentagon-based layered material featuring a narrow band gap in its monolayer and metallicity in its bulk,[27] we systematically study the electronic structure of penta-NiN_2 multilayers and unveil its potential in metallic sliding ferroelectricity.

2. Computational Details

Our calculations are performed by using the Vienna ab initio simulations package (VASP)[28,29] based on density functional theory,

---

C. Hou, Q. Wang
School of Materials Science and Engineering
Peking University
Beijing 100871, China
E-mail: qianwang2@pku.edu.cn

Y. Shen
Materials Genome Institute
Shanghai University
Shanghai 200444, China

The ORCID identification number(s) for the author(s) of this article can be found under https://doi.org/10.1002/adfm.202421311

DOI: 10.1002/adfm.202421311

where the projector augmented wave method[30] is used for describing the interaction between valence electrons and ion cores, and the plane waves with an energy cutoff of 600 eV are used to expand the electron wave functions. The exchange–correlation interaction among the valence electrons is calculated by the Perdew–Burke–Ernzerhof (PBE) functional[31] within the generalized gradient approximation.[32] The vacuum space of 15 Å is adopted to avoid the interactions between the adjacent cells in the out-of-plane direction. The first Brillouin zone is sampled by a Monkhorst–Pack k-point mesh[33] with the grid density of $2\pi \times 0.02$ Å^{-1}. All the structures are fully optimized with a convergence threshold of 1×10^{-4} eV Å^{-1} for force and 1×10^{-6} eV for energy. The Heyd–Scuseria–Ernzerhof (HSE06) hybrid functional is used for calculating the electronic band structures.[34] The optB86b-vdW functional is considered for all the calculations to deal with the effect of vdW interactions in the layered penta-NiN$_2$.[35] The finite displacement method[36] implemented in the Phonopy code[37] is used for calculating the phonon spectra of single- and multi-layer penta-NiN$_2$ using their $4 \times 4 \times 1$ supercells. Ab initio molecular dynamics (AIMD) simulations for these systems are performed using the canonical ensemble with a Nosé–Hoover thermostat.[38] The ferroelectric switching pathway is computed by using the climbing-image nudged elastic band (CI-NEB) method.[39]

For metallic 2D layered structures, finite dipole moment in the out-of-plane direction is calculated by an integration of the electronic and ionic charge density as well defined by the classical dipole method.[40] The ionic vertical polarization can be calculated by using the following formula from the point charge model:

$$P_{ion} = \frac{e}{S}\sum_i z_i Q_i = \frac{e}{S}\bar{z}_{ion} n \tag{1}$$

where S is the in-plane area of the unit cell, e is the elementary charge, z_i is the spatial position of the ith ion along the z direction, Q_i is the ionic charge of the ith ion, n is the total number of electrons, and $\bar{z}_{ion}$ represents the ion center (positive charge center) of the system in the z direction. The sum is over all ions in the unit cell.

The electronic vertical polarization is calculated using the following integral over the whole unit cell:

$$P_e = -\frac{e}{S}\iint\int z\rho(\mathbf{r})d\mathbf{r} \tag{2}$$

where $\rho(\mathbf{r})$ represents the electronic charge density.

The total vertical polarization is the sum of the ion polarization and the electron polarization,

$$P_z = P_{ion} + P_e = \frac{e}{S}\sum_i z_i Q_i - \frac{e}{S}\iint\int z\rho(\mathbf{r})d\mathbf{r} \tag{3}$$

where the direction is from the negative charge center to the positive charge center.

The SHG susceptibility $\chi^{(2)}$ $abc(\omega)$ is calculated within the independent particle approximation[41] by using the package developed by Zhang's group,[42] where a, b, $c \in \{x, y, z\}$. The SHG tensor is expressed by the sum of contributions from the pure inter-band susceptibility $\chi(2)$ abc,e (ω) and the mixed inter-band and intra-band susceptibility $\chi(2)$ abc,i (ω), which are calculated by using the following formulas:

$$\chi^{(2)}_{abc,e}(\omega) = \frac{e^3}{\hbar^2\Omega}\sum_{nml,k}\frac{r^a_{nm}\{r^a_{nm}r^b_{ml}r^c_{ln}\}}{(\omega_{ln}-\omega_{ml})}\left[\frac{2f_{mn}}{\omega_{mn}-2\omega}+\frac{f_{ln}}{\omega_{ln}-2\omega}+\frac{f_{ml}}{\omega_{ml}-\omega}\right] \tag{4}$$

$$\chi^{(2)}_{abc,i}(\omega) = \frac{i}{2}\frac{e^3}{\hbar^2\Omega}\sum_{nm,k} f_{nm}\left[\begin{array}{l}\frac{2}{\omega_{mn}(\omega_{mn}-2\omega)}r^a_{nm}(r^b_{nm;c}+r^c_{mn;b})+\\ \frac{1}{\omega_{mn}(\omega_{mn}-\omega)}(r^a_{nm;c}r^b_{mn}+r^a_{nm;b}r^c_{mn})+\\ \frac{1}{\omega^2_{mn}}\left(\frac{1}{\omega_{mn}-\omega}-\frac{4}{\omega_{mn}-2\omega}\right)r^a_{nm}(r^b_{mn}\Delta^c_{mn}+r^c_{mn}\Delta^b_{mn})\\ -\frac{1}{2\omega_{mn}(\omega_{mn}-2\omega)}(r^b_{nm;a}r^c_{mn}+r^c_{nm;a}r^b_{mn})\end{array}\right]. \tag{5}$$

Here, Ω is the volume of the periodic cell, which is the area of the 2D unit cell. $f_{nm} = f_n - f_m$, $\omega_{nm} = \omega_n - \omega_m$, and $\Delta_{nm} = v_{nn} - v_{mm}$ are the differences of the Fermi distribution function, energy, and electronic group velocity between the nth and mth bands, respectively, which are deduced from the electronic structure. ra $mn = pa$ $mn/im\omega_{mn}$ is the position operator r_{mn} projected on the a direction, p_{mn} is the momentum matrix component, $\{rb$ $nlra$ $lm\}$ is defined as $1/2(rb$ $nlra$ $lm+$ ra $nlrb$ $lm)$, and rb $nm;a$ is the generalized derivative of the position operator in the momentum space expressed as:

$$r^b_{nm;a} = \frac{r^a_{nm}\Delta^b_{mn}+r^b_{nm}\Delta^a_{mn}}{\omega_{nm}}+\frac{i}{\omega_{nm}}\sum_l(\omega_{lm}r^a_{nl}r^b_{lm}-\omega_{nl}r^b_{nl}r^a_{lm}). \tag{6}$$

The static SHG susceptibility is obtained from the Kramers–Kronig transformation,[43]

$$\chi^{(2)}_{abc}(0) = \mathrm{Re}[\chi^{(2)}_{abc}(0)] = \frac{2}{\pi}P\int_0^\infty\{\mathrm{Im}[\chi^{(2)}_{abc}(\omega)]/\omega\}d\omega. \tag{7}$$

3. Results and Discussion

3.1. Geometry and Stability

Before constructing multilayered configurations of penta-NiN$_2$, we test the accuracy of our calculations for the geometry, electronic structure, and dynamical stability of its monolayer sheet, which are in perfect consistence with the previous study,[44] as shown in Figure S1 (Supporting Information). According to the bilayer stacking ferroelectricity (BSF) theory,[16] monolayer penta-NiN$_2$ belongs to the $P4/mbm$ (no. 63) layer group, its corresponding bilayer configuration remains centrosymmetric and nonpolarized upon sliding. Thus, trilayer penta-NiN$_2$ is the simplest stacking configuration that could exhibit sliding ferroelectricity, whose properties could represent the common nature of sliding ferroelectricity for all thicker multilayers. Given the semiconducting nature of monolayer penta-NiN$_2$ and the metallic nature of its bulk counterpart (Figure S2, Supporting Information), multilayer penta-NiN$_2$ would serve as the playground for studying metallic sliding ferroelectricity, since the band gap of 2D semiconductors typically diminishes with increasing number of layers. To explore the configuration space of trilayer penta-NiN$_2$, we fixed the middle layer and respectively slid the upper and bottom layers by using $\boldsymbol{r}_{\text{up}} = (m\boldsymbol{a} + n\boldsymbol{b})/10$ and $\boldsymbol{r}_{\text{bot}} = (p\boldsymbol{a} + q\boldsymbol{b})/10$ from the commonly denoted AAA stacking pattern according to the stacking misalignment rule,[45] where $\boldsymbol{a}$ and $\boldsymbol{b}$ are the lattice vectors as shown in **Figure 1a**, and m, n, p, $q \in \{0, 1, 2, 3, 4, 5, 6, 7,$

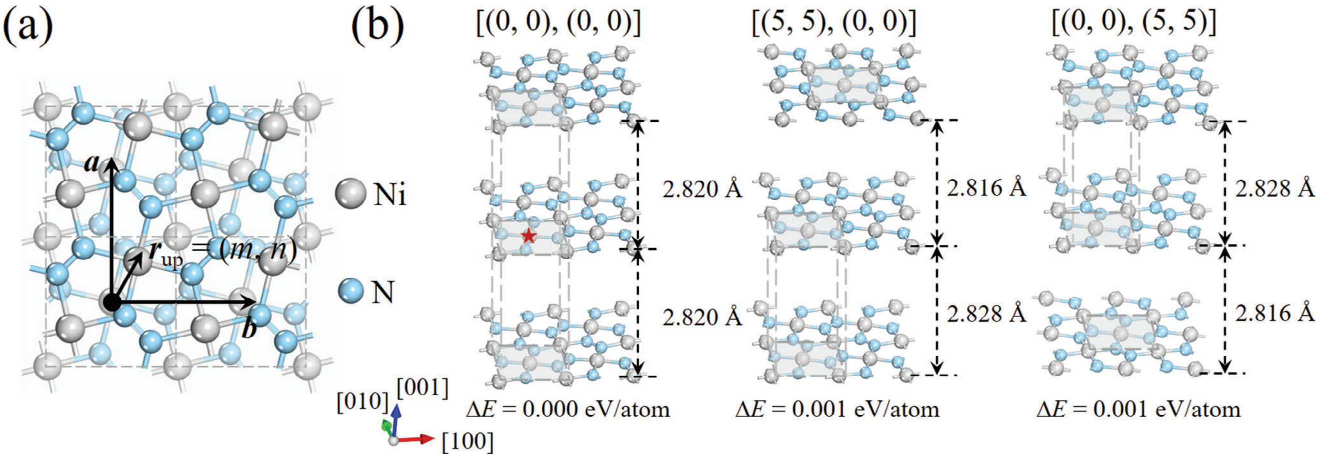

Figure 1. a) Sliding pattern of the stacked configuration of the trilayer penta-NiN_2. b) The stable stacking patterns of the trilayer penta-NiN_2. The red star denotes a center of inversion symmetry. The optimized interlayer distances are also provided.

8, 9}. The resulting slid stacking patterns are denoted as [(*m*, *n*), (*p*, *q*)]. The configuration space of the trilayer penta-NiN_2 (10^4) is reduced to 1260 possible sliding patterns by considering the symmetry constraints, which are shown in Supplementary Note 1 in the SI. After geometry optimization, four distinct stacking patterns, namely [(0, 0), (0, 0)], [(5, 5), (0, 0)], [(0, 0), (5, 5)], and [(5, 5), (5, 5)] are identified. The AAA pattern, [(0, 0), (0, 0)], is found to be the ground-state configuration with its total energy lower by 0.001, 0.001, and 0.002 eV per atom than that of the [(5, 5), (0, 0)], [(0, 0), (5, 5)], and [(5, 5), (5, 5)] configurations, respectively. Next, we calculated the phonon spectra of the four different stacked patterns to check their dynamic stability. The configurations of [(0, 0), (0, 0)], [(5, 5), (0, 0)], and [(0, 0), (5, 5)] are found to be dynamically stable as no any imaginary phonon modes are present throughout their first Brillouin zones (see Figure S3, Supporting Information). While the [(5, 5), (5, 5)] configuration is dynamically unstable with some imaginary phonon modes around the Γ point, as illustrated in Figure S4 (Supporting Information). The geometries of the stable stacking configurations and interlayer distances are shown in Figure 1b. To further investigate the thermal stability of the three dynamically stable configurations, we performed ab initio molecular dynamics (AIMD) simulations at 300, 600, and 900 K, respectively, with a duration of 10 ps and a time step of 1 fs for each simulation. To avoid the "fake" stability caused by the constraints of periodic boundary conditions, a 3 × 3 × 1 supercell was used in these simulations. As shown in Figure S5 (Supporting Information), the total potential energies of the supercells fluctuate around constant values during the simulations at 900 K, and their geometries do not suffer significant distortion at the end of simulations, indicating that the [(0, 0), (0, 0)], [(5, 5), (0, 0)], and [(0, 0), (5, 5)] sliding configurations are all thermally stable at temperatures up to 900 K. Based on a comprehensive examination of possible magnetic ordering, trilayer penta-NiN_2 is found to be non-magnetic, which is consistent with the fact that the penta-NiN_2 monolayer itself is nonmagnetic.[27] More details can be found in Supplementary Note 2 in the SI.

Since stable stacking patterns were found only when one layer is shifted, we next explored the potential energy surface (PES) associated with interlayer sliding, we identified that these stable stacking patterns correspond to local energy minima, as shown in **Figure 2**a. Thus, among all the possible stacking configurations of trilayer penta-NiN_2, the [(0, 0), (0, 0)], [(5, 5), (0, 0)], and [(0, 0), (5, 5)] stacking configurations are dynamically and thermally stable, consistent with their coincidence with local minima on the PES. Despite the interlayer vdW interaction with a magnitude of 0.1 eV/atom obtained from the energy difference between monolayer and trilayer penta-NiN_2, the PES of the trilayer penta-NiN_2 is relatively flat with a maximum energy fluctuation of 0.035 eV/atom, as expected for vdW interactions between flat 2D sheets. We also conducted a symmetry analysis of trilayer penta-NiN_2, as shown in Figure 2b. There are three shifting vectors, G (0, 0),

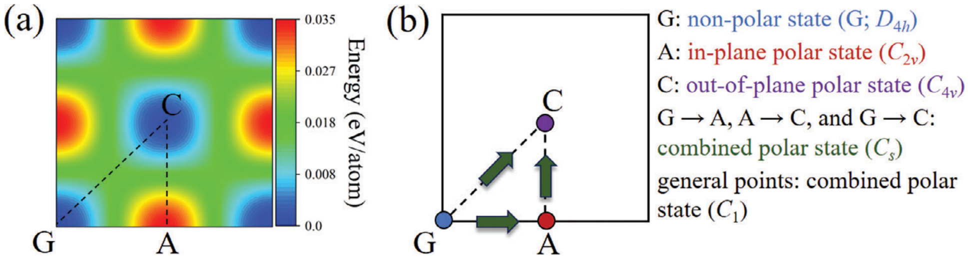

Figure 2. a) Potential energy surface associated with the interlayer sliding of the trilayer penta-NiN_2. The color scale refers to the energy range of the PES corrugation (in eV/atom). b) Symmetry analysis of the trilayer penta-NiN_2 correlated by the identity symmetry.

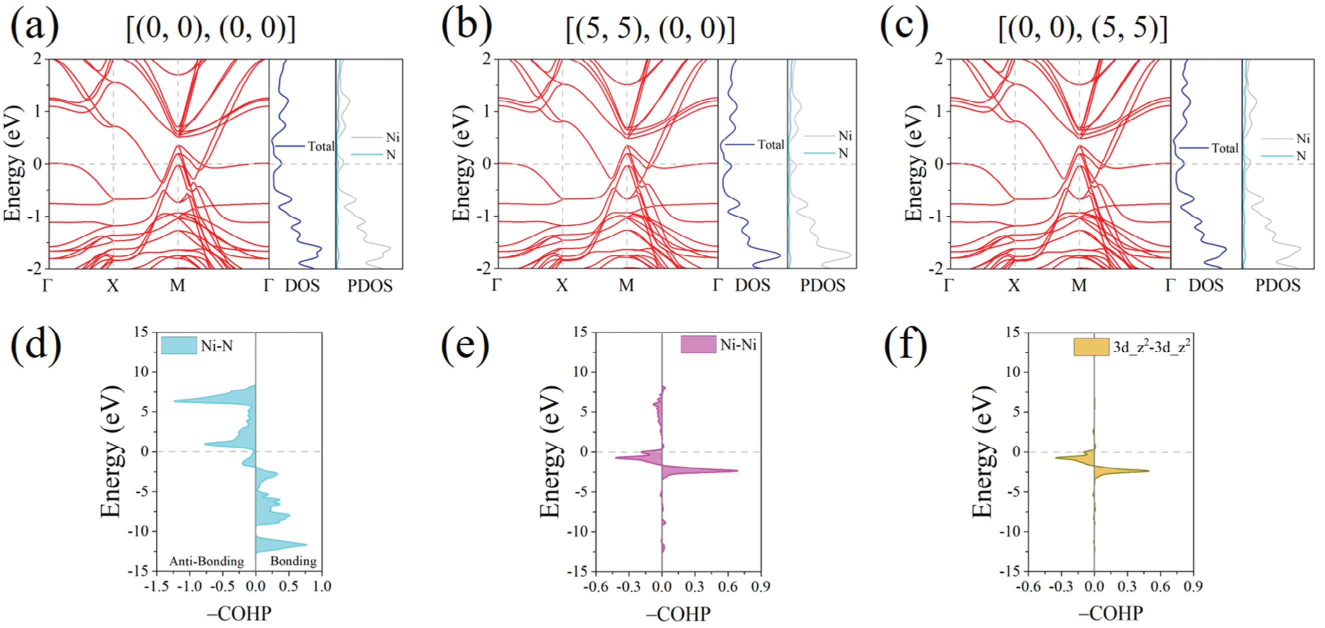

Figure 3. a–c) Electronic band structures, DOS, and PDOS calculated at the HSE06 level of the stable stacking patterns of the trilayer penta-NiN_2. d–f) COHP analysis of the Ni—N bond, Ni atoms in the adjacent layer and 3d_z^2 orbitals of Ni atoms in the adjacent layer on the [(0, 0), (0, 0)] stacking configuration of the trilayer penta-NiN_2.

A ($\frac{1}{2}a$, 0), C ($\frac{1}{2}a$, $\frac{1}{2}b$), which leads to three typical stacking configurations. The trilayer stacked AAA stacking pattern, labeled as G, exhibits no polarization with the D_{4h} symmetry and corresponds to the global energy minimum. In contrast, shifting either the top or bottom layer by C ($\frac{1}{2}a$, $\frac{1}{2}b$) breaks the mirror symmetry at the interface for inducing the out-of-plane polarization, which also corresponds to a global energy minimum. The [(0, 0), (0, 0)] stacking pattern, with inversion symmetry, is non-polar, while, the symmetry of the [(5, 5), (0, 0)] and [(0, 0), (5, 5)] stacking patterns are broken by the adjacent interlayer configurations. These stacking patterns exhibit out-of-plane polarizations under C_{4v} symmetry with polar states correlated with the mirror symmetry, resulting in opposite out-of-plane polarizations. For future experimental characterization, the simulated scanning tunneling microscopy (STM) images and X-ray diffraction (XRD) patterns for the three stable sliding configurations of trilayer penta-NiN_2 are provided in Figure S7 (Supporting Information).

3.2. Electronic Properties and Spontaneous Polarization

To investigate the electronic properties of trilayer penta-NiN_2 in its stable sliding configurations [(0, 0), (0, 0)], [(5, 5), (0, 0)] and [(0, 0), (5, 5)], we calculated the band structures and corresponding total and partial density of states (DOS) at the HSE06 level. As plotted in **Figures** 3a–c, one can see that the energy bands cross the Fermi level along the X-M and M-Γ paths, demonstrating that all three configurations are intrinsically metallic. The projected DOS (PDOS) analysis reveals that the metallicity is mainly contributed from the orbitals of Ni atoms. This is further confirmed by analyzing crystal orbital Hamilton population (COHP),[46,47] as shown in Figures 3d–f, where the negative COHP (right) represents the bonding contribution, while the positive COHP (left) stands for the anti-bonding contribution. By examining the interactions involving Ni atoms in the trilayer penta-NiN_2 with the [(0, 0), (0, 0)] stacking pattern, one can see that in the trilayer penta-NiN_2, the energies of the bonding orbitals of the Ni—N bonds are consistently lower than those of the anti-bonding orbitals, as shown in Figure 3d. Therefore, the

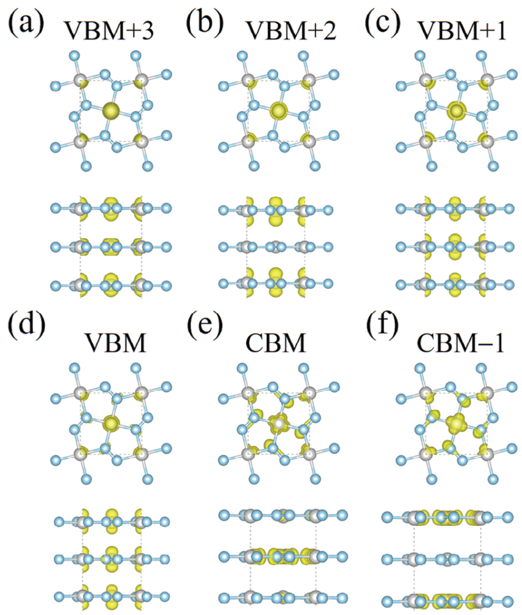

Figure 4. a–f) Band-decomposed charge density of energy bands near the Fermi level on the M point in the Brillouin zone of the [(0, 0), (0, 0)] stacking configuration of the trilayer penta-NiN_2. All valance bands (a-d) feature Ni 3d_z^2 orbitals. The isosurface values are ± 0.007 Å^{-3}.

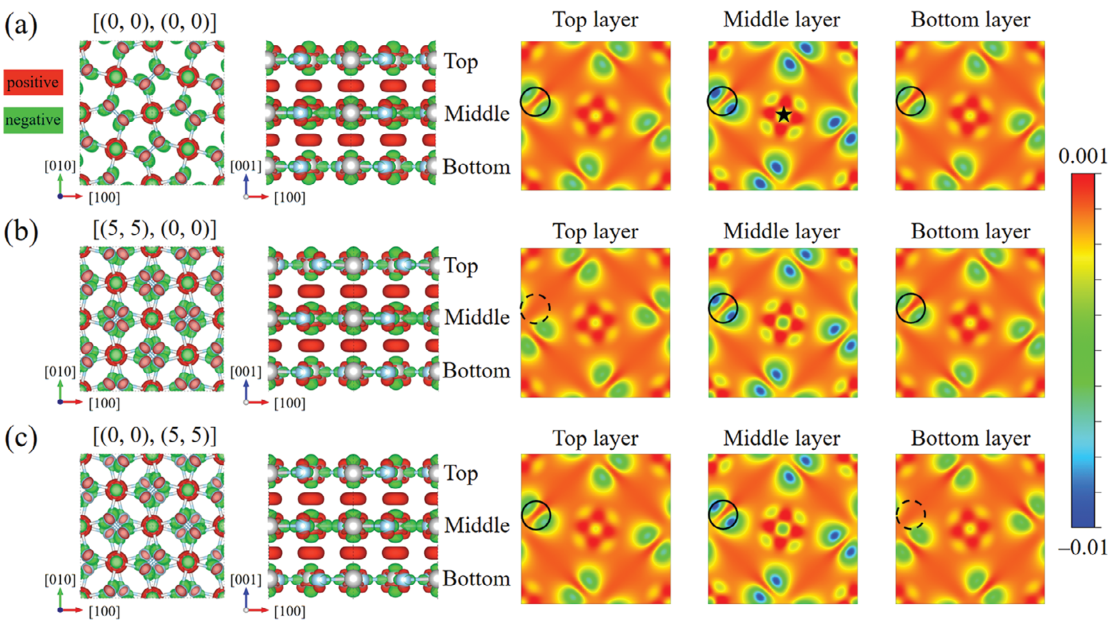

Figure 5. Spatial distribution of the deformation charge density and its slices across the given planes in a) [(0, 0), (0, 0)], (b) [(5, 5), (0, 0)], and (c) [(0, 0), (5, 5)] stacking configurations of trilayer penta-NiN_2. The isosurface values for spatial distribution are ± 0.007 $Å^{-3}$, with red and green regions representing charge gain and loss, respectively. The black star in the middle-layer slice of (a) denotes a center of inversion symmetry. The solid and dashed black circles centered at relative coordinates (0.10, 0.60) in each slice represent the existence and absence of the N atom, respectively.

Ni-N bonds contribute less to metallicity. In contrast, for the interactions between the nearest-neighbor Ni atoms in adjacent layers, some bonding orbitals possess higher energy than the anti-bonding orbitals due to the overlapping of their $3d\_z^2$ orbitals, as shown in Figures 3e,f, and evidenced by the band-decomposed charge densities in **Figures** 4a–f, resulting in metallic property for the trilayer penta-NiN_2. Different from the trilayer, the bonding orbitals always possess higher energy than the anti-bonding orbitals in the monolayer and bilayer penta-NiN_2, making these layers semiconducting (see Figure S8, Supporting Information). Thus, it is clear that the metallic properties of the trilayer penta-NiN_2 originate from the interactions of $3d\_z^2$ orbitals of Ni atoms.

In addition to the metallic features, the magnitude of spontaneous polarization is another crucial indicator for the performance of metallic sliding ferroelectricity in electronic devices. The [(0, 0), (0, 0)] configuration exhibits D_{4h} symmetry, which ensures the simultaneous presence of both in-plane and out-of-plane symmetry. Consequently, the spontaneous polarization in this configuration is zero. Conversely, the [(5, 5), (0, 0)] and [(0, 0), (5, 5)] configurations exhibit C_{4v} symmetry, indicating that their spontaneous polarization along the out-of-plane direction is non-zero. The calculated P_z values for the [(5, 5), (0, 0)] and [(0, 0), (5, 5)] configurations are 5.39×10^{-13} and -5.39×10^{-13} C m^{-1}, respectively. These values are equal in magnitude but opposite in direction, suggesting the presence of out-of-plane sliding ferroelectricity in trilayer penta-NiN_2.

To gain a better understanding of spontaneous polarization switching in trilayer penta-NiN_2 with different sliding configurations, we analyzed their deformation charge densities. The deformation charge densities for the three configurations are plotted in **Figure** 5. The symmetry breaking in the charge redistributions of the [(5, 5), (0, 0)] and [(0, 0), (5, 5)] configurations are evident in the deformation charge density values on the planes defined by the Ni atoms in respective penta-NiN_2 layers. The charge redistribution slices for [(0, 0), (0, 0)] is consistent with the mirror symmetry M_z and inversion symmetry in this system. However, after sliding trilayer penta-NiN_2 from the [(0, 0), (0, 0)] configuration to either [(5, 5), (0, 0)] or [(0, 0), (5, 5)], both symmetries are broken. Typically, the green regions for charge accumulation around N atoms in the stationary layers, highlighted by the solid black circles in Figures 5b,c, are vertically mapped to the orange regions for charge depletion in empty space in the sliding layers. Such mapping is in line with the emergence of out-of-plane spontaneous polarization, which points from the charge-cumulated middle layer to the charge–depleted sliding layer, i.e., upward in the [(5, 5), (0, 0)] configuration and downward in the [(0, 0), (5, 5)] configuration. This mechanism extends the atomic mechanism proposed for bilayer *h*-BN, where polarization originates from charge redistribution in the $2p_z$ orbitals of N atoms, as is the case with the polar AB and BA stacking patterns in bilayer *h*-BN.[11] The interlayer interaction energy of the trilayer penta-NiN_2 configuration, obtained from the energy difference between monolayer and trilayer penta-NiN_2, is 0.1 eV/atom, which is not uniformly distributed over all atoms but rather concentrated on the Ni atoms, as supported by the charge accumulation between Ni atoms shown in Figure 5. The VBM and CBM of the monolayer penta-NiN_2, originated from the Ni orbitals,[27] can be significantly altered by the moderate interlayer Ni-atom interaction, leading to metallicity in trilayer penta-NiN_2.

Such analysis is supported by the Bader charge analysis[48,49] where the charge transfer is asymmetric with the sliding layer

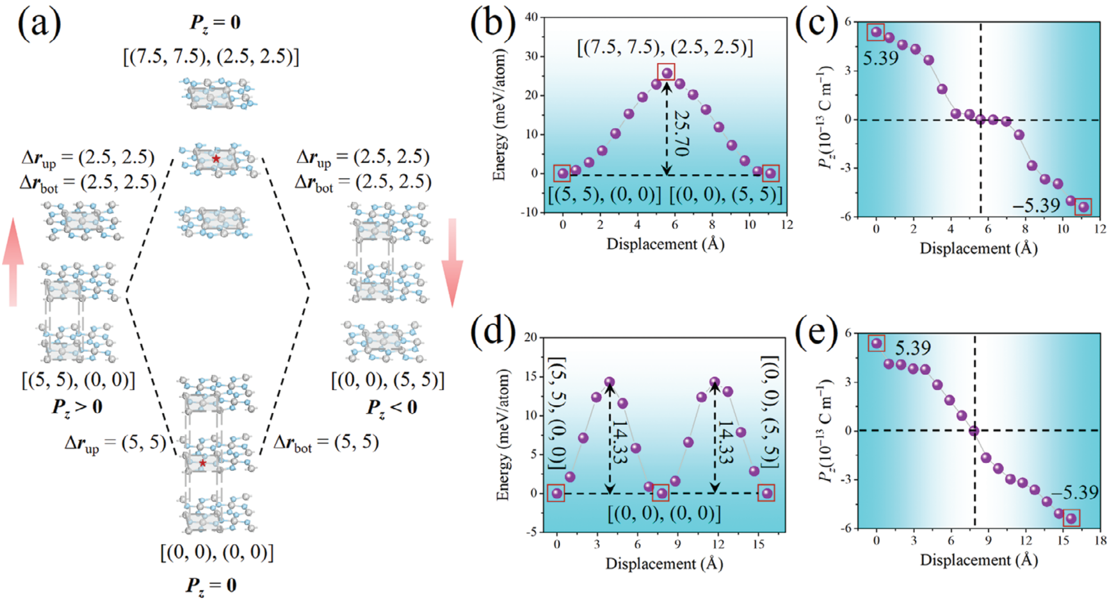

Figure 6. a) The sliding patterns of the trilayer penta-NiN_2 with their spontaneous polarization along the out-of-plane direction, with the red arrow indicating the direction of out-of-plane polarization. b,d) Energy profile and c,e) spontaneous polarization P_z along the [001] direction as a function of the sliding displacement between the [(5, 5), (0, 0)] and [(0, 0), (5, 5)] stacking configurations of the trilayer penta-NiN_2.

loses more electrons, as shown in Figure S9 (Supporting Information), attributed to the short interlayer distances between the sliding layer and the middle layer in trilayer penta-NiN_2. Consequently, metallic sliding ferroelectricity is realized in trilayer penta-NiN_2, with the [(5, 5), (0, 0)] and [(0, 0), (5, 5)] patterns exhibiting opposite out-of-plane spontaneous polarizations.

3.3. Sliding Ferroelectricity

For device application, the ferroelectric switching barrier is a key parameter measuring the energy consumption involved in polarization switching. As discussed above, the spontaneous polarization along the out-of-plane direction can be switched upon interlayer sliding in the trilayer penta-NiN_2. This switching is facilitated by the two stable energetically degenerate sliding configurations, namely, the [(5, 5), (0, 0)] and [(0, 0), (5, 5)] patterns, as shown in **Figure** 6a. We examined two possible sliding paths between the [(5, 5), (0, 0)] and [(0, 0), (5, 5)] configurations. The first path considered is a direct sliding process, which leads to a ferroelectric polarization switching barrier of 25.70 meV atom, as shown in Figure 6b. The transition state identified by the CI-NEB algorism is the [(7.5, 7.5), (2.5, 2.5)] pattern, which possesses C_{2h} symmetry shown in Figure 6a, indicating polarization along the out-of-plane direction with inversion symmetry.

The second path considered is an indirect sliding process mediated by the stable energetically degenerate [(0, 0), (0, 0)] configuration. We divided the path into two segments, and respectively calculated the energy barriers for the transition from the [(0, 0), (0, 0)] configuration to the [(5, 5), (0, 0)] and [(0, 0), (5, 5)] configurations, as depicted in Figure 6d. In this case, the process requires a lower ferroelectric polarization switching barrier of 14.33 meV/atom compared with that of the direct sliding process, making it the most feasible path for the trilayer penta-NiN_2. The polarization switching processes for both direct and indirect sliding processes of the trilayer penta-NiN_2 are shown in Figures 6c,e, which evolves from $P_z = 5.39 \times 10^{-13}$ C m^{-1} in the [(5, 5), (0, 0)] configuration to $P_z = 0$ C m^{-1} in the [(0, 0), (0, 0)] or [(7.5, 7.5), (2.5, 2.5)] configuration, and then to $P_z = -5.39 \times 10^{-13}$ C m^{-1} in the [(0, 0), (5, 5)] configuration. A comparison is presented in **Table** 1 for the polarization switching energy barrier and ferroelectric polarization value of trilayer penta-NiN_2 with those of several other metallic sliding ferroelectric materials studied previously. It shows that the penta-NiN_2 possesses a larger ferroelectric polarization value than WTe_2,[13,18] $PtTe_2$,[50] $PdTe_2$,[50] and $NiTe_2$,[50] suggesting its advantages for applications in practical devices.

We further investigate the origin of sliding ferroelectricity in trilayer penta-NiN_2, corresponding to the previously discussed direct and indirect sliding processes, as shown in Figure S10 (Supporting Information). The stacking patterns of [(5, 5), (0, 0)] and [(0, 0), (5, 5)] with the intrinsic mirror

Table 1. Comparison of the polarization switching energy barrier (in meV/atom) and ferroelectric polarization value (in 10^{-13} C m^{-1}) of the trilayer penta-NiN_2 with those of some other metallic sliding ferroelectric materials.

structure	metal or semiconductor	energy barrier	polarization
penta-NiN_2	metal	14.33	±5.39
WTe_2[13,18]	metal	≈0.2	±2.20
$PtTe_2$[50]	metal	18.67	±4.60
$PdTe_2$[50]	metal	10.67	±0.60
$NiTe_2$[50]	metal	7.33	±5.20

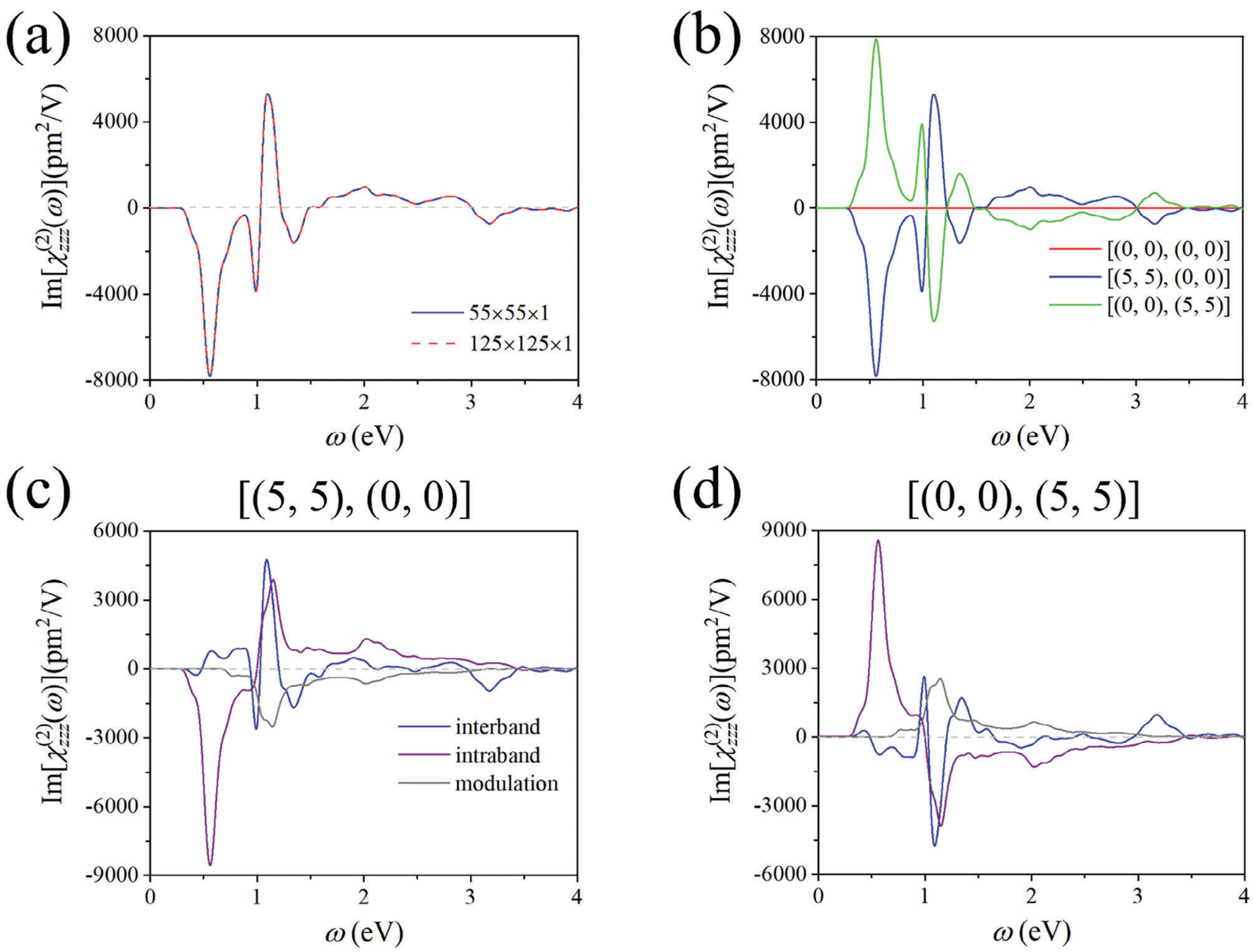

Figure 7. a) Imaginary part of the SHG susceptibility $\mathrm{Im}[\chi(2)\ zzz(\omega)]$ of the trilayer penta-NiN$_2$ with the [(5, 5), (0, 0)] stacking configuration with different *k*-mesh. b) Imaginary part of the SHG susceptibilities $\mathrm{Im}[\chi(2)\ zzz(\omega)]$, and c,d) corresponding interband, intraband, and modulation contributions of the trilayer penta-NiN$_2$ with the [(0, 0), (0, 0)], [(5, 5), (0, 0)], and [(0, 0), (5, 5)] stacking configurations.

symmetry exhibit C_{4v} symmetry, resulting in the opposite out-of-plane polarization. For the indirect process, the two opposing ferroelectric states (+*m*Fe and –*m*Fe) in trilayer penta-NiN$_2$ are transformed via a glide plane operation $\{M_z|0\}$. The intermediate paraelectric state (PE) in the [(0, 0), (0, 0)] configuration possesses D_{4h} point group, leading to the vanishing of its out-of-plane polarization. For the direct process, the two opposing ferroelectric states (+*i*Fe and –*i*Fe) are related through an inversion operation $\{I|0\}$. The intermediate PE state in the [(7.5, 7.5), (2.5, 2.5)] configuration possesses C_{2h} point group, and its out-of-plane polarization also vanishes due to inversion symmetry.

As the number of layers increases, the possible stacking configurations increase exponentially.[51] For simplicity, we assume that the same sliding mechanism is applicable to the four- and five-layered penta-NiN$_2$, and then find the out-of-plane ferroelectric sliding polarization of $\pm$ 7.52 $\times$ 10^{-13} C m^{-1} and $\pm$ 6.47 $\times$ 10^{-13} C m^{-1}, respectively, as shown in Figure S11 (Supporting Information). We further find that the polarization switching barriers decrease with an increasing number of layers in multilayer penta-NiN$_2$, as shown in Figure S12 (Supporting Information). However, as the number of layers increases, the required external electric field to penetrate the polar metal to induce polarization switching increases, ultimately leading to the loss of ferroelectricity.

3.4. Second Harmonic Generation

In order to facilitate the experimental characterization, we calculated the second harmonic generation (SHG) that emerges as an effective method for characterizing sliding ferroelectric phase transitions due to its non-destructive nature, high stability, tunability, ultrafast response, polarization sensitivity, and simplicity.[10] For SHG properties of the trilayer penta-NiN$_2$ with the [(0, 0), (0, 0)], [(5, 5), (0, 0)], and [(0, 0), (5, 5)] stacking patterns, we show the converged results in **Figure 7**, calculated by using a *k*-point mesh of 55 × 55 × 1 with the detailed convergence test given in Figure 7a. The calculated static SHG susceptibilities $\chi(2)\ zzz(0)$ of the [(0, 0), (0, 0)], [(5, 5), (0, 0)], and [(0, 0), (5, 5)] configurations are summarized in **Table 2**. It is known that the SHG susceptibility strongly relies on the symmetry of materials. After sliding the trilayer penta-NiN$_2$ from [(0, 0), (0, 0)]

Table 2. Static SHG susceptibilities $\chi(2)$ $zzz(0)$ (pm^2/V) of the trilayer penta-NiN$_2$ with the [(0, 0), (0, 0)], [(5, 5), (0, 0)], and [(0, 0), (5, 5)] sliding configurations.

configuration	$\chi(2)$ $zzz(0)$
[(0, 0), (0, 0)]	0
[(5, 5), (0, 0)]	−1545.98
[(0, 0), (5, 5)]	1545.98

configuration to [(5, 5), (0, 0)] and [(0, 0), (5, 5)] configuration, the symmetry reduces from the centrosymmetric $P4/mbm$ symmetry (space group no. 127) to $P4bm$ polar symmetry (space group no. 100), leading to the emergency of SHG responses. One can see that for the $\chi(2)$ $zzz(0)$ components, the SHG response of the [(5, 5), (0, 0)] and [(0, 0), (5, 5)] configuration configurations have the same absolute value of 1545.98 pm^2/V, but in opposite directions. This result is consistent with the reversed spontaneous polarization between these two configurations.

We then calculated the frequency-dependent SHG susceptibility of the [(0, 0), (0, 0)], [(5, 5), (0, 0)], and [(0, 0), (5, 5)] configurations, as shown in Figure 7b. According to Equation 7, the low-energy region of Im[$\chi(2)$ $zzz(\omega)$] primarily influences the value of $\chi(2)$ $zzz(0)$ due to the presence of the denominator ω in the integrand. Hence, we focused on the low-energy peaks in each Im[$\chi(2)$ $zzz(\omega)$], which make dominant contributions to $\chi(2)$ $zzz(0)$. It is notable that the curves of Im[$\chi(2)$ $zzz(\omega)$] in the [(5, 5), (0, 0)] and [(0, 0), (5, 5)] configurations exhibit similar shapes, but with opposite trends. For the [(5, 5), (0, 0)] configuration, the initial peaks of Im[$\chi(2)$ $zzz(\omega)$] are −7852.95, −3905.32, and 5270.24 pm^2/V at 0.56, 0.99, and 1.10 eV, respectively. In contrast, the first several peaks in the [(0, 0), (5, 5)] configuration are 7852.95, 3905.32, and −5270.24 pm^2/V at 0.56, 0.99, and 1.10 eV, respectively. Since the crystal structure of [(0, 0), (0, 0)] configuration is centrosymmetric, it cannot exhibit any SHG response. As shown in Figures 7c,d, we plotted the different contributions to the Im[$\chi(2)$ $zzz(\omega)$] of the [(5, 5), (0, 0)] and [(0, 0), (5, 5)] configurations, showing that the inter-band and intra-band contributions to each SHG susceptibilities in the low-energy region tend to oppose each other, and the major peaks are mainly contributed by the intra-band term. Hence, the intra-band contribution to each SHG susceptibilities is larger in magnitude compared to that from the inter-band contribution. Such significant contrast in SHG response between the different stable configurations would simplify the experimental characterization of the sliding ferroelectric phase transition in trilayer penta-NiN$_2$.

4. Conclusion

In summary, by performing a state-of-the-art theoretical study on the metallic sliding ferroelectricity of trilayer penta-NiN$_2$, we identified three stable sliding configurations from the scanned configuration space and demonstrated that trilayer penta-NiN$_2$ exhibits metallic sliding ferroelectricity along the out-of-plane direction with a low polarization switching barrier of 14.33 meV/atom. Notably, the trilayer penta-NiN$_2$ possesses two stable polar states of [(5, 5), (0, 0)] and [(0, 0), (5, 5)], which exhibit reversible spontaneous polarization of $\pm 5.39 \times 10^{-13}$ C m^{-1}. Significant changes in the second harmonic generation of these polar states are found for facilitating the experimental characterization of the sliding. This study shows the potential of pentagonal 2D materials as metallic sliding ferroelectrics by going beyond the traditional 2D systems and would encourage experimental investigation in this direction.

Supporting Information

Supporting Information is available from the Wiley Online Library or from the author.

Acknowledgements

This work is partially supported by grants from the National Natural Science Foundation of China (Grant No. NSFC-12274007) and is also supported by the High-Performance Computing Platform of Peking University, China.

Conflict of Interest

The authors declare no conflict of interest.

Data Availability Statement

The data that support the findings of this study are available from the corresponding author upon reasonable request.

Keywords

first-principles calculations, metallic ferroelectricity, pentagon-based materials, sliding ferroelectricity

Received: November 5, 2024
Revised: December 14, 2024

---

[1] R. Fei, W. Kang, L. Yang, *Phys. Rev. Lett.* **2016**, *117*, 097601.
[2] F. Liu, L. You, K. L. Seyler, X. Li, P. Yu, J. Lin, X. Wang, J. Zhou, H. Wang, H. He, S. T. Pantelides, W. Zhou, P. Sharma, X. Xu, P. M. Ajayan, J. Wang, Z. Liu, *Nat. Commun.* **2016**, *7*, 12357.
[3] C. Zheng, L. Yu, L. Zhu, J. L. Collins, D. Kim, Y. Lou, C. Xu, M. Li, Z. Wei, Y. Zhang, M. T. Edmonds, S. Li, J. Seidel, Y. Zhu, J. Z. Liu, W. X. Tang, M. S. Fuhrer, *Sci. Adv.* **2018**, *4*, eaar7720.
[4] K. Chang, J. Liu, H. Lin, N. Wang, K. Zhao, A. Zhang, F. Jin, Y. Zhong, X. Hu, W. Duan, Q. Zhang, L. Fu, Q. K. Xue, X. Chen, S. H. Ji, *Science* **2016**, *353*, 274.
[5] K. Chang, F. Küster, B. J. Miller, J. R. Ji, J. L. Zhang, P. Sessi, S. Barraza-Lopez, S. S. P. Parkin, *Nano Lett.* **2020**, *20*, 6590.
[6] L. Li, M. Wu, *ACS Nano* **2017**, *11*, 6382.
[7] M. Wu, J. Li, *Proc. Natl. Acad. Sci. U.S.A.* **2021**, *118*, 2115703118.
[8] H. Jiang, L. Li, Y. Wu, R. Duan, K. Yi, L. Wu, C. Zhu, L. Luo, M. Xu, L. Zheng, X. Gan, W. Zhao, X. Wang, Z. Liu, *Adv. Mater.* **2024**, *36*, 2400670.
[9] R. Bian, R. He, E. Pan, Z. Li, G. Cao, P. Meng, J. Chen, Q. Liu, Z. Zhong, W. Li, F. Liu, *Science* **2024**, *385*, 57.
[10] L. P. Miao, N. Ding, N. Wang, C. Shi, H. Y. Ye, L. Li, Y. F. Yao, S. Dong, Y. Zhang, *Nat. Mater.* **2022**, *21*, 1158.

[11] K. Yasuda, X. Wang, K. Watanabe, T. Taniguchi, P. Jarillo-Herrero, *Science* **2021**, *372*, 1458.
[12] F. Sui, M. Jin, Y. Zhang, R. Qi, Y. N. Wu, R. Huang, F. Yue, J. Chu, *Nat. Commun.* **2023**, *14*, 36.
[13] Z. Fei, W. Zhao, T. A. Palomaki, B. Sun, M. K. Miller, Z. Zhao, J. Yan, X. Xu, D. H. Cobden, *Nature* **2018**, *560*, 336.
[14] S. Deb, W. Cao, N. Raab, K. Watanabe, T. Taniguchi, M. Goldstein, L. Kronik, M. Urbakh, O. Hod, M. Ben Shalom, *Nature* **2022**, *612*, 465.
[15] A. Jindal, A. Saha, Z. Li, T. Taniguchi, K. Watanabe, J. C. Hone, T. Birol, R. M. Fernandes, C. R. Dean, A. N. Pasupathy, D. A. Rhodes, *Nature* **2023**, *613*, 48.
[16] J. Ji, G. Yu, C. Xu, H. J. Xiang, *Phys. Rev. Lett.* **2023**, *130*, 146801.
[17] H. Wang, X. Qian, *NPJ Comput. Mater.* **2019**, *5*, 119.
[18] Q. Yang, M. Wu, J. Li, *J. Phys. Chem. Lett.* **2018**, *9*, 7160.
[19] S. Zhang, J. Zhou, Q. Wang, X. Chen, Y. Kawazoe, P. Jena, *Proc. Natl. Acad. Sci. U.S.A.* **2015**, *112*, 2372.
[20] Y. Shen, Q. Wang, *Database for pentagon-based sheets* http://www.pubsd.com/.
[21] Y. Shen, Q. Wang, *Phys. Rep.* **2022**, *964*, 1.
[22] Y. Guo, J. Zhou, H. Xie, Y. Chen, Q. Wang, *NPJ Comput. Mater.* **2022**, *8*, 40.
[23] J. Xin, Y. Guo, Q. Wang, *Phys. Rev. Mater.* **2023**, *7*, 074001.
[24] Y. Guo, C. Zhang, J. Zhou, Q. Wang, P. Jena, *Phys. Rev. Appl.* **2019**, *11*, 064063.
[25] C. Hou, Y. Shen, Q. Wang, A. Yoshikawa, Y. Kawazoe, P. Jena, *ACS Nano* **2024**, *18*, 16923.
[26] L. Liu, Y. Ji, M. Bianchi, S. M. Hus, Z. Li, R. Balog, J. A. Miwa, P. Hofmann, A. P. Li, D. Y. Zemlyanov, Y. Li, Y. P. Chen, *Nat. Mater.* **2024**, *23*, 1339.
[27] M. Bykov, E. Bykova, A. V. Ponomareva, F. Tasnádi, S. Chariton, V. B. Prakapenka, K. Glazyrin, J. S. Smith, M. F. Mahmood, I. A. Abrikosov, A. F. Goncharov, *ACS Nano* **2021**, *15*, 13539.
[28] G. Kresse, J. Furthmüller, *Phys. Rev. B* **1996**, *54*, 11169.
[29] G. Kresse, J. Furthmüller, *Comp. Mater. Sci.* **1996**, *6*, 15.
[30] P. E. Blöchl, *Phys. Rev. B* **1994**, *50*, 17953.
[31] J. P. Perdew, K. Burke, M. Ernzerhof, *Phys. Rev. Lett.* **1996**, *77*, 3865.
[32] M. P. Teter, M. C. Payne, D. C. Allan, *Phys. Rev. B* **1989**, *40*, 12255.
[33] H. J. Monkhorst, J. D. Pack, *Phys. Rev. B* **1976**, *13*, 5188.
[34] J. Heyd, G. E. Scuseria, M. Ernzerhof, *J. Chem. Phys.* **2003**, *118*, 8207.
[35] J. Klimeš, D. R. Bowler, A. Michaelides, *Phys. Rev. B* **2011**, *83*, 195131.
[36] K. Parlinski, Z. Q. Li, Y. Kawazoe, *Phys. Rev. Lett.* **1997**, *78*, 4063.
[37] A. Togo, I. Tanaka, *Scr. Mater.* **2015**, *108*, 1.
[38] S. Nosé, *J. Chem. Phys.* **1984**, *81*, 511.
[39] G. Mills, H. Jónsson, *Phys. Rev. Lett.* **1994**, *72*, 1124.
[40] W. Ding, J. Zhu, Z. Wang, Y. Gao, D. Xiao, Y. Gu, Z. Zhang, W. Zhu, *Nat. Commun.* **2017**, *8*, 14956.
[41] J. E. Sipe, E. Ghahramani, *Phys. Rev. B* **1993**, *48*, 11705.
[42] Z. Fang, J. Lin, R. Liu, P. Liu, Y. Li, X. Huang, K. Ding, L. Ning, Y. Zhang, *CrystEngComm* **2014**, *16*, 10569.
[43] S. N. Rashkeev, W. R. L. Lambrecht, *Phys. Rev. B* **2001**, *63*, 165212.
[44] J. H. Yuan, Y. Q. Song, Q. Chen, K. H. Xue, X. S. Miao, *Appl. Surf. Sci.* **2019**, *469*, 456.
[45] Z. G. Yu, Y. W. Zhang, *J. Appl. Phys.* **2015**, *118*, 165706.
[46] R. Nelson, C. Ertural, J. George, V. L. Deringer, G. Hautier, R. Dronskowski, *J. Comput. Chem.* **2020**, *41*, 1931.
[47] V. L. Deringer, A. L. Tchougréeff, R. Dronskowski, *J. Phys. Chem. A* **2011**, *115*, 5461.
[48] G. Henkelman, A. Arnaldsson, H. Jónsson, *Comput. Mater. Sci.* **2006**, *36*, 354.
[49] W. Tang, E. Sanville, G. Henkelman, *J. Phys. Condens. Matter.* **2009**, *21*, 084204.
[50] H. Sheng, Z. Fang, Z. Wang, *Phys. Rev. B* **2023**, *108*, 104109.
[51] L. Yang, S. Ding, J. Gao, M. Wu, *Phys. Rev. Lett.* **2023**, *131*, 096801.